ISSN 1648-7788 / eISSN 1822-4180

VILNIUS TECH
Vilnius Gediminas Technical University

AVIATION

2026
Volume 30
Issue 4
Pages 263–277
https://doi.org/10.3846/aviation.2026.28140

DEVELOPMENT AND VALIDATION OF A UAV-BORNE NAI(TL) SCINTILLATION SYSTEM FOR ENVIRONMENTAL RADIATION SURVEYING: A METHODOLOGICAL APPROACH

Jonas MISIŪNAS [1]✉, Dominykas PETRULAITIS [2], Laurynas ARŠTIKYS [3], Dainius JASAITIS [4], Aleksandr PROKOPČIK [5]

[1, 4]*Department of Aviation Technologies, Antanas Gustaitis' Aviation Institute, Vilnius Gediminas Technical University, Linkmenų g. 28, LT-08217 Vilnius, Lithuania*
[2, 3]*Department of Aeronautical Engineering, Antanas Gustaitis' Aviation Institute, Vilnius Gediminas Technical University, Linkmenų g. 28, LT-08217 Vilnius, Lithuania*
[5]*Division for Laboratory Investigations, Ignalina Nuclear Power Plant, LT-31152 Drūkšinių vil., Visaginas, Lithuania*

Article History:
- received 5 June 2026
- accepted 17 June 2026

Abstract. Unmanned aerial vehicles (UAVs) are progressively employed for environmental radiation assessment, providing swift, low-altitude surveillance of regions that are hazardous or inaccessible for ground personnel. This study details the creation and methodological validation of a UAV-mounted gamma-ray spectrometry system utilizing a 2-inch NaI(Tl) scintillation detector incorporated into a multi-rotor platform. The detector underwent calibration at an accredited laboratory utilizing collimated ^{241}Am, ^{137}Cs, and ^{60}Co sources, resulting in a three-point quadratic energy calibration with an energy resolution of 6.19% FWHM at 661.7 keV. Pre-flight bench experiments evaluated detector stability under operational settings by comparing background spectra with motors deactivated, motors activated without propellers (electromagnetic interference), and motors activated with propellers (combined interference and vibration). The detector and propulsion system utilize a single battery via a regulated converter, exemplifying a worst-case scenario. Motor operation resulted in negligible alterations in count rate (<0.4%) or dead time, indicating both electromagnetic and mechanical resilience without the need for supplementary shielding or vibration isolation. The minimum detectable activity for ^{137}Cs was assessed in relation to survey altitude, indicating the trade-off between area coverage and sensitivity for mission design. The findings validate that the integrated system satisfies the metrological standards for environmental gamma surveying.

Keywords: UAV-borne gamma spectrometry, NaI(Tl) detector, electromagnetic interference, vibration testing, minimum detectable activity, radiological monitoring.

✉Corresponding author. E-mail: *jonas.misiunas@vilniustech.lt*

1. Introduction

Ionizing radiation hazards represent a persistent challenge for environmental safety and public health, arising from nuclear accidents, naturally occurring radioactive materials (NORM), improperly disposed industrial or medical sources, or legacy contamination such as that associated with the Chernobyl and Fukushima disasters. According to the International Atomic Energy Agency (IAEA), 4,243 incidents involving nuclear and radioactive materials were registered in the Incident and Trafficking Database (ITDB) between 1993 and 2024, with 147 reported in 2024 alone (International Atomic Energy Agency, 2026). Conventional ground-based survey methods are constrained by the need for direct human presence in hazardous areas, limited spatial coverage, and reduced practicality in complex terrain – limitations that are particularly acute in post-accident scenarios where large areas must be rapidly characterized while minimizing operator dose (Connor et al., 2020). While manned aerial spectrometry (using helicopters or light aircraft) can cover larger areas, it introduces prohibitive operational costs, substantial logistical footprints, and inherent risks to the flight crew, while remaining restricted by minimum safe altitude regulations that compromise spatial resolution over complex topography. Unmanned aerial vehicles (UAVs) have emerged as a compelling alternative for airborne radiation surveying. By elevating the detector above the terrain, they decouple the measurement from direct human exposure, enable rapid coverage of inaccessible areas, and allow systematic, repeatable flight paths. The potential of this approach was demonstrated following the 2011 Fukushima Daiichi accident, when UAV-borne gamma detection systems mapped dose-rate

Copyright © 2026 The Author(s). Published by Vilnius Gediminas Technical University

This is an Open Access article distributed under the terms of the Creative Commons Attribution License (*http://creativecommons.org/licenses/by/4.0/*), which permits unrestricted use, distribution, and reproduction in any medium, provided the original author and source are credited.

distributions across the exclusion zone with safety margins unattainable by ground crews (Sanada et al., 2016). The field has since expanded considerably, with more than 350 peer-reviewed publications addressing UAV applications in radiological monitoring as of 2022 (Ardiny et al., 2024). Among the detector technologies suitable for airborne deployment, NaI(Tl) scintillation detectors occupy a central position, combining high detection efficiency, adequate energy resolution, low mass, and cost-effectiveness (Kunze et al., 2022). However, integrating a NaI(Tl) detector into a UAV platform introduces non-trivial engineering challenges: electromagnetic interference (EMI) from brushless motors and electronic speed controllers (ESCs) can degrade spectral quality, mechanical vibration may affect photomultiplier tube (PMT) gain stability, and temperature variation can induce spectral drift. These factors must be characterized and mitigated before a system can be considered fit for operational surveys. Despite the extensive literature on UAV-based radiation monitoring, most studies focus on a specific algorithmic or operational aspect, or present results from systems that are already fully flight-qualified. Comparatively few publications document the complete development pipeline – from laboratory detector characterization, through UAV integration, to structured pre-flight validation – which limits the reproducibility and transferability of such systems. The present study addresses this gap by reporting the development and validation of a custom UAV-borne NaI(Tl) scintillation system for environmental gamma radiation surveying. A multi-rotor platform was selected for its manoeuvrability and hovering capability. Crucially, to bridge the gap between laboratory physics and airborne engineering, this work introduces a structured bench-test verification protocol designed to isolate and quantify the systemic effects of airframe vibrations and motor-induced EMI on the spectroscopic output. The primary contribution of this work is a replicable methodological framework, spanning from accredited laboratory baseline calibration to pre-flight bench validation under simulated operational conditions, serving as a rigorous engineering foundation to guarantee telemetry integrity before executing full flight trials.

2. UAV radiation surveying: theoretical framework and integration challenges

2.1. UAV platforms for airborne radiation monitoring

Three principal UAV configurations have been applied to airborne radiation surveying: fixed-wing, single-rotor, and multi-rotor systems, each offering a distinct aerodynamic and operational trade-off between coverage area, flight endurance, payload capacity, and logistical flexibility (International Atomic Energy Agency, 2022). Fixed-wing UAVs excel at rapidly covering large, contaminated areas owing to their high cruise speeds and extended flight endurance. They have been successfully deployed to map macro-level residual contamination across the Chernobyl exclusion zone (Connor et al., 2020) and for wide-area radiological surveillance with NaI(Tl) payloads (Geelen et al., 2022). However, their inability to hover, the requirement for relatively high minimum safe altitudes (approximately 150 m) to mitigate terrain collision risks, and their dependence on specialised launch and recovery infrastructure (such as runways or catapults) severely limit their utility for localised, high-resolution surveys and low-altitude point-source detection. Single-rotor UAVs (unmanned helicopters) offer significantly higher payload capacities and can operate effectively at lower tactical altitudes of 50 to 100 m. For instance, Sanada and Torii (2015) utilized a heavy-lift Yamaha RMAX helicopter to map complex dose-rate distributions around the Fukushima Daiichi facility, while Jiang et al. (2016) leveraged the superior lifting power of a single-rotor platform to deploy a heavy Compton camera for three-dimensional radiation source imaging. Despite these advantages, single-rotor systems suffer from high mechanical complexity, substantial procurement and maintenance costs, and the requirement for highly skilled remote pilots, which restricts their widespread operational deployment (Towler et al., 2012). Multi-rotor UAVs (e.g., quadcopters, hexacopters) have consequently emerged as the most widely adopted platform type for localised aero radioecological missions. Their capacity for precise hovering, low-speed tactical flight, and Vertical Take-Off and Landing (VTOL) operations without field infrastructure makes them uniquely suited for high-resolution localised surveys, complex urban monitoring, and orphan source searches. In past field campaigns, multi-rotor platforms have generated high-fidelity 3D contamination maps (Martin et al., 2016) and localised lost sources with positional errors of only a few tens of centimetres (Gong et al., 2019). The primary limitations of multi-rotor systems are their shorter flight endurance (typically 20–45 min) and restricted payload capacity (often capped at 2–5 kg), which may preclude the use of massive, large-volume detector arrays (Martin et al., 2020; MacFarlane et al., 2014). However, for compact spectroscopic configurations, this payload envelope is entirely sufficient. A multi-rotor platform was therefore selected for the present study, balancing the need for tight altitude control, hovering capability over anomalies, and rapid deployment flexibility.

2.2. Radiation detector technologies for UAV integration

The selection of a radiation detector for UAV deployment is governed by a strict optimization matrix comprising competing severe requirements: high intrinsic detection sensitivity, adequate energy resolution for isotopic identification, minimal power consumption, mechanical robustness against flight-induced shocks, and strict mass constraints to conform to the UAV's payload limits. Three principal detector classes have been critically evaluated in the literature for airborne integration (International

Atomic Energy Agency, 2022; Ardiny et al., 2024). Gas-filled detectors, primarily Geiger-Müller (GM) counters, represent a highly robust and lightweight solution. They are mechanically shock-resistant and provide a direct, real-time measure of gross gamma count rates or total dose rates. However, GM tubes lack spectroscopic capability completely, they cannot resolve photon energy distributions, making it impossible to differentiate between benign natural background fluctuations (NORM) and anthropogenic contamination. Consequently, they are inadequate as primary sensors for comprehensive environmental characterisation (Ardiny et al., 2024). Semiconductor detectors offer excellent energy resolution but present severe operational bottlenecks for multi-rotor deployment. High-Purity Germanium (HPGe) detectors provide the best standard in resolution, but they require cryo-cooling systems (liquid nitrogen or mechanical cryocoolers), driving total payload masses well above 20 kg and demanding high power, which restricts them to large, specialised manned or unmanned aircraft. Cadmium Zinc Telluride (CZT) semiconductors operate efficiently at ambient temperatures and are lightweight, but their crystallisation process limits individual sensor volumes. To achieve high detection efficiency at operational flight altitudes, large and prohibitively expensive CZT arrays are required, limiting their widespread transferability (International Atomic Energy Agency, 2022). Scintillation detectors occupy the optimal position for UAV-based gamma surveying, balancing efficiency, resolution, mass, and cost. Within this class, Thallium-doped Sodium Iodide NaI(Tl) remains the long-established reference standard for airborne radiometry due to its large available volumes and high light yield. Other scintillators present specific drawbacks: Caesium Iodide CsI(Tl) offers superior mechanical shock resistance, but inferior energy resolution compared to NaI(Tl). Conversely, newer lanthanide-halide crystals, such as Lanthanum Bromide $LaBr_3$(Ce) and Cerium Bromide $CeBr_3$, provide outstanding energy resolution (<3% at 662 keV) but are highly hygroscopic, fragile, and substantially more expensive. Furthermore, $LaBr_3$ exhibits an intrinsic self-activity background from the primordial isotope ^{138}La, which introduces spectral anomalies and complicates low-level environmental monitoring during brief aerial tracking windows (International Atomic Energy Agency, 2022).

2.3. NaI(Tl) as the reference standard for airborne gamma spectrometry

NaI(Tl) scintillation detectors have occupied a central role in airborne gamma spectrometry for decades, and this position has been maintained in the UAV era. (Kunze et al., 2022) developed and validated a UAV-based NaI(Tl) gamma spectrometry system for uranium legacy sites in Central Asia, demonstrating that the high light yield of the crystal allows for meaningful, high-resolution environmental characterization under dynamic field conditions. Similarly, Bunn et al. (2022) benchmarked NaI(Tl)-equipped hexarotor measurements against ground-based measurements using ^{60}Co, ^{137}Cs, and ^{241}Am sources, identifying flight altitude as the critical parameter governing detection sensitivity. A critical design choice in modern airborne scintillation systems concerns the photosensor coupled to the crystal: traditional Photomultiplier Tubes (PMTs) versus solid-state Silicon Photomultipliers (SiPMs). Although SiPMs have been increasingly proposed as a shock-resistant and low-voltage alternative for tactical field applications, PMT-based configurations remain predominant for large-volume crystals in airborne environmental sensing (International Atomic Energy Agency, 2022). SiPM arrays coupled to large scintillators (such as 2'' × 2'' or greater) introduce substantial dark noise due to the cumulative capacitance of the interconnected microcells and exhibit severe gain temperature dependence, which degrades energy resolution during open-air flight profiles. Consequently, PMT electronics remain the reference standard due to their mature temperature stabilization protocols, linear energy response, and superior signal-to-noise ratios. However, because a PMT relies on a fragile, vacuum-sealed glass envelope housing a high-voltage dynode structure, its integration into an active airframe necessitates rigorous characterization of mechanical and electrical isolation, as detailed below.

2.4. Airborne integration challenges: flight dynamics, EMI, and environmental effects

Integrating a NaI(Tl) detector into a multi-rotor UAV introduces instrumentation challenges with no counterpart in ground-based deployments, arising from three principal disturbance sources: flight dynamics, electromagnetic emissions, and environmental fluctuations. The first challenge involves the geometric attenuation and atmospheric absorption of gamma quanta during dynamic flight. As a multi-rotor UAV alters its altitude h above the ground, the expected photon flux $I(h)$ decreases non-linearly according to the combined effects of the inverse-square law and atmospheric attenuation (Corbacho et al., 2024):

$$I(h) = I_0 \frac{e^{-\mu h}}{4\pi h^2}, \quad (1)$$

where I_0 is the source intensity and μ is the air linear attenuation coefficient for a given gamma energy. This operating environment requires precise altitude hold and real-time geometric correction algorithms. Furthermore, the spatial resolution of the survey is bounded by the flight velocity v and the integration sampling time Δt of the Multichannel Analyser (MCA). If the UAV velocity is too high relative to the accumulation interval, the resulting spatial radiation mapping suffers from directional blurring, compromising localised source identification.

Beyond flight dynamics, hardware integration introduces severe electromagnetic interference (EMI) from high-current brushless motors and Electronic Speed Controllers (ESCs). ESCs typically operate via Pulse Width Modulation (PWM) at switching frequencies ranging from 16 kHz to 32 kHz. This rapid switching generates high-frequency broadband noise that easily couples into the PMT high-voltage supply or high-impedance preamplifier stages, producing spurious low-energy counts, baseline displacement, and spectral degradation (International Atomic Energy Agency, 2022).

Simultaneously, mechanical vibration transmitted through the airframe from the propellers introduces microphonic noise within the PMT assembly and can physically degrade the crystal-to-PMT optical coupling, resulting in artificial broadening of the Full Width at Half Maximum (FWHM) and gain instability (Vetter et al., 2018). Hence, anti-vibration mounting is widely recommended. Finally, environmental temperature gradients during flight induce spectral drift due to the temperature-dependent light yield of the NaI(Tl) crystal (approximately 0.2–0.3% per °C) and PMT gain variations (Knoll, 2010). Most published studies report final system performance without documenting the isolated contribution of each disturbance mechanism, making it difficult to design appropriate countermeasures. The present study addresses this through a structured bench-test protocol that separates EMI and vibration effects via controlled motor activation sequences prior to full flight trials.

2.5. Comparative overview of reported UAV gamma-spectrometry systems

The systems reviewed above illustrate how strongly UAV gamma-spectrometry configurations are shaped by their mission profile. Table 1 summarises representative platforms in terms of detector size, payload mass, survey altitude, and demonstrated capability. The configurations span three orders of magnitude in detector volume – from 1 cm^3 CZT crystals on lightweight multi-rotors optimised for metre-scale spatial resolution, to 0.13 L $LaBr_3$(Ce) assemblies on 100 kg-class helicopters optimised for wide-area coverage – with the choice of detector, platform, and altitude in each case reflecting a deliberate trade-off between resolution, sensitivity, and coverage.

Viewed together, these studies are predominantly application-driven: their emphasis lies on operational outcomes such as radiation maps, localization accuracy, or campaign results, with the underlying detector integration treated as an established starting point. The present work adopts a complementary perspective and focuses on the development pathway itself – the sequence of traceable calibration, interference verification, and detection-limit budgeting through which a detector–platform combination becomes survey-ready. The system of Gong et al. (2019), which employs the same ORTEC 905-3 detector model, illustrates how naturally the two perspectives connect: operational capabilities such as source-localization algorithms build directly on the detector-level characterisation documented here.

Table 1. Representative UAV-borne gamma-spectrometry systems reported in the literature. n/r – not reported

System	Platform	Detector (type, size)	Survey altitude	Primary application and reported performance
MacFarlane et al. (2014), Martin et al. (2016)	Lightweight multi-rotor (AARM)	CZT (Kromek GR1), 1 cm^3	< 3–15 m	Rapid, metre-scale-resolution mapping of localised anomalies and contaminant distribution, demonstrates the reach of ultra-compact detectors at very low altitude
Sanada and Torii (2015)	Single-rotor unmanned helicopter (RMAX G1), ~100 kg class	3 × $LaBr_3$(Ce), 38.1 × 38.1 mm (0.13 L total)	50–80 m	Wide-area dose-rate mapping of the Fukushima exclusion zone, large payload capacity supporting high-volume, high-resolution spectrometry
Gong et al. (2019)	Octocopter (RotorRAD)	NaI(Tl) 2″ × 2″ (ORTEC 905-3) + GM tube	≈1 m (localization trials)	Localization of lost radioactive sources by a dedicated search algorithm, achieving metre-level positioning accuracy at low altitude
Schraml et al. (2022)	RiCOPTER-M (15 kg payload capacity)	Scintillator + GM gamma probe (GAMON Drone), 9.25 kg sensor bundle incl. LiDAR	up to 150 m	Real-time localization of IAEA category 3–4 sources with 3D-LiDAR terrain fusion, mean positioning accuracy 17.1 m over 500 × 500 m areas
Corbacho et al. (2024)	Multi-rotor	$LaBr_3$(Ce)	n/r	Activity quantification of point and extended sources with overall uncertainties of the order of 20%
This work	Custom quadrotor, ~5 kg total take-off mass	NaI(Tl) 2″ × 2″ (ORTEC 905-3) + digiBASE-RH (~0.7 kg spectrometric payload)	2 m nominal, extrapolated to 30 m	Metrological development pipeline: accredited calibration (6.19% FWHM at 661.7 keV), pre-flight EMI/vibration verification, MDA 43.8 ± 1.7 kBq (^{137}Cs, 300 s, 2 m) with altitude scaling

3. Methodology and experimental setup

3.1. Detector selection and technical specifications

The sensor selected for this study is the ORTEC 905-3 NaI(Tl) scintillation detector, comprising a 2″ × 2″ (51 mm × 51 mm) thallium-doped sodium iodide crystal coupled to a 2-inch diameter PMT. The detector operates across an energy range of approximately 30 keV to 3 MeV, encompassing the principal gamma-ray emissions of naturally occurring radionuclides (NORM) – including ^{40}K at 1460.8 keV and members of the ^{238}U and ^{232}Th decay series – as well as anthropogenic isotopes of radiological significance such as ^{137}Cs (661.7 keV) and ^{60}Co (1173.2 and 1332.5 keV). Signal acquisition is performed using an ORTEC *digiBASE*-RH integrated spectroscopic module – a 14-pin PMT base incorporating a programmable high-voltage bias supply, charge-sensitive preamplifier, digital signal processor (DSP), multichannel analyser (MCA), and USB interface within a single compact housing. From an aviation engineering perspective, this integrated architecture eliminates the requirement for separate, bulky NIM-bin electronics modules, thereby drastically reducing the system payload mass to a total assembly weight of approximately 0.7 kg. Furthermore, the entire spectroscopic payload is powered directly via a standard USB 2.0 interface, drawing less than 500 mW of power. This ultra-low power consumption minimizes the thermal load and avoids penalizing the UAV's onboard battery power budget, directly preserving the aircraft's operational flight endurance. The complete assembly specifications are summarized in Table 2.

Table 2. NaI(Tl) detector and spectroscopic electronics specifications

Parameter	Value / Description
Detector model	ORTEC 905-3
Crystal material	NaI(Tl)
Crystal dimensions	2″ × 2″ (51 mm × 51 mm)
PMT diameter	2 inches
Energy range	~30 keV – 3 MeV
Energy resolution (662 keV)	< 7.0% FWHM (manufacturer specification)
Spectroscopic module	ORTEC *digiBASE*-RH
Integrated components	HV supply, preamplifier, DSP, MCA, USB
Interface	USB 2.0 (direct to PC)
Acquisition software	ORTEC MAESTRO

3.2. Laboratory calibration setup

Detector characterisation measurements were performed at the accredited Verification and Calibration Laboratory of the Ignalina Nuclear Power Plant (INPP), Lithuania, using a collimated UPGD-2M-D gamma-ray calibration unit (Figure 1) – a metrological installation designed for the calibration of radiation dosimeters and spectrometers using a highly collimated gamma beam. The unit incorporates a shielded collimator housing a rotating drum magazine that holds up to four sealed gamma-ray sources, the required source is selected and positioned in the collimation channel by means of a manual rotation rod. For the present work, the drum was loaded with ^{241}Am, ^{137}C and ^{60}Co sources (nominal dimensions Ø20 × 40 mm), allowing multi-point energy calibration spanning 59.5–1332.5 keV under identical collimated-beam geometry. The detector is mounted on a movable carriage that travels along a graduated rail, allowing reproducible positioning at source-to-detector distances of up to 3500 mm, with positioning accuracy governed by the inverse-square-law deviation of ±2.5%. The detector centreline is fixed at 740 mm above the platform and aligned with the collimated beam axis using an integrated laser sight. From a methodological standpoint, establishing this rigid, scattering-free collimated geometry is essential to isolate the intrinsic detector characteristics from environmental scatter. This laboratory configuration provides the baseline energy and efficiency reference scale, which is required before evaluating the sensor's performance under the complex, non-collimated 2π geometry encountered during actual open-air UAV flights.

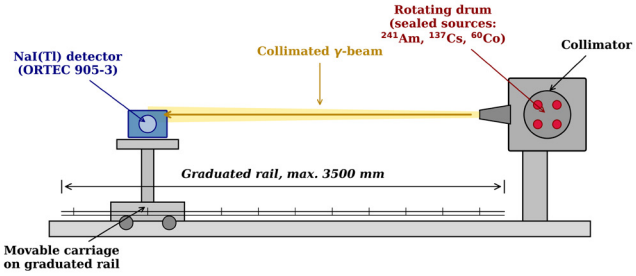


Figure 1. Schematic of the UPGD-2M-D collimated gamma-ray calibration unit used for NaI(Tl) detector characterization at the accredited INPP Verification and Calibration Laboratory

3.3. Calibration and efficiency evaluation procedures

The experimental methodology requires a rigorous three-stage computational procedure to transform the raw multichannel analyser (MCA) digital outputs into metrologically traceable spectroscopic data: energy calibration, resolution characterization, and absolute peak efficiency evaluation. The first stage involves establishing a mathematically robust relation between the MCA channel number *Ch* and the incident gamma-ray photon energy *E*. Spectral peak centroids for the primary photopeaks of ^{241}Am (59.54 keV), ^{137}Cs (661.7 keV), and ^{60}Co (1173.2 and 1332.5 keV) were determined by fitting an analytical Gaussian function superimposed on a linear background. The energy calibration curve was subsequently modelled using the second-

order polynomial to account for minor non-linearities in the PMT and MCA electronics (Gilmore & Joss, 2024):

$$E(Ch) = a_0 + a_1 \cdot Ch + a_2 \cdot Ch^2, \quad (2)$$

where a_0, a_1, and a_2 are the empirically derived calibration coefficients optimized via least-squares regression. The quadratic term accounts for the known slight non-linearity of the PMT response at higher energies (Knoll, 2010).

To assess the effect of counting statistics on measured resolution, three spectra of a ^{137}Cs source were acquired at a fixed distance of 200 cm with live times of 5 s, 60 s, and 300 s. FWHM values were determined by Gaussian fitting within the MAESTRO analysis engine.

Absolute full-energy peak efficiency ε relates the net peak count rate to the certified source activity. The measurement was performed at a source-to-detector distance of 200 cm – corresponding to the nominal operating altitude of the multi-rotor UAV during environmental survey configurations. The absolute efficiency is calculated as (Gilmore & Joss, 2024):

$$\varepsilon = \frac{N_{net}}{A \cdot Y_\gamma \cdot t}, \quad (3)$$

where N_{net} is the net full-energy peak area (counts), A is the source activity at the time of measurement (Bq), Y_γ is the gamma-ray emission probability per disintegration, and t is the live measurement time (s).

Finally, a laboratory background characterization was conducted with an empty collimator channel over 1802 s (30 min) to establish a clean reference baseline and evaluate external environmental interferences before coupling the payload to the airframe.

3.4. System architecture and UAV integration

Before executing airborne surveys, a systematic pre-flight validation was conducted to determine whether operation of the UAV propulsion and power systems affects the NaI(Tl) detector response. Rather than performing a live flight, the fully integrated aircraft was held in a stationary ground-test configuration, allowing controlled, repeatable data collection and the isolation of specific disturbance sources that would otherwise be obscured by flight dynamics. The integrated platform is a custom-built quadrotor UAV with a 0.6 m × 0.6 m motor-to-motor frame, 17-inch propellers, and a total mass of approximately 5 kg. The aircraft was raised on rigid 2 m support legs, bringing the airframe's apex to approximately 2.6 m above the ground and placing the nadir-mounted detector at a source-to-ground distance of 2.0 m. This geometry replicates the standard low-altitude hovering configuration of the multi-rotor platform during environmental surveys, ensuring that the validation accurately reflects operational survey conditions. In this rigidly affixed configuration, the crystal centre is separated from the lower section of the airframe – specifically, the onboard battery – by approximately 16 cm.

Throughout the test, the detector drew power from the UAV's single onboard battery, reproducing the operational power architecture in which the detector and propulsion system share a common source. The 6S battery (22.2 V nominal) was first routed through an inline power-measuring module to log voltage and current draw. Its output was then fed to the first DC-DC converter, which stepped the 22 V rail down to 15 V, followed by the second DC-DC converter – incorporating additional protection circuitry – that further regulated the supply to 12 V. This 12 V output was soldered to a USB-C power cable supplying the *Latte Panda* companion computer, which in turn powered the *digiBASE*-RH spectroscopic module and PMT. This staged, doubly regulated chain ensures that battery voltage fluctuations during discharge do not propagate to the detector bias, eliminating supply-induced spectral drift as a confounding variable. Because the detector and propulsion system are powered from the same battery, the measurement inherently captures both conducted electrical interference along the shared power rail and radiated emissions from the motors, electronic speed controllers, and flight electronics. The test therefore constitutes a conservative, worst-case evaluation of system robustness.

3.5. Pre-flight validation setup and procedure

The validation was performed outdoors under a natural gamma background with no calibration source present. The overall bench-test arrangement is shown in Figure 2, and a close-up view of the detector mounting is shown in Figure 3. The comparison therefore relies on the ambient background spectrum, and the same energy calibration



Figure 2. Overall view of the bench-test setup: the UAV mounted on a fixed 2 m platform in flight configuration



Figure 3. Close-up view showing the NaI(Tl) detector hard-mounted on the UAV airframe

was retained across all acquisitions. The primary objective was to determine whether the electromagnetic emissions of the UAV exert any significant influence on the PMT-based spectroscopic measurements.

Three operating conditions were analysed sequentially, each recorded in triplicate over a 600 s acquisition:

Motors deactivated (*OFF*, *baseline*): all drone electronics powered down, establishing the undisturbed detector reference.

Motors activated, *no propellers* (*EMI*): motors energised and rotating without propellers, isolating the purely electromagnetic contribution of the motors, electronic speed controllers, and flight electronics in the absence of mechanical excitation.

Motors activated, *propellers installed* (*EMI + vibration*): propellers affixed and motors engaged to produce reverse thrust, exerting downward pressure on the aircraft and thereby superimposing airframe vibration onto the electromagnetic interference to simulate the combined stresses encountered during flight.

In both powered conditions the motors were driven at approximately 50% throttle, representative of hovering flight. The current draw quantifies the electrical load imposed in each case. With propellers removed (EMI), the three runs drew 1.81 A, 1.85 A, and 1.96 A (mean 1.87 A). With propellers fitted, the draw rose to 33.9 A, 35.26 A, and 34.09 A (mean 34.42 A). This approximately eighteen-fold increase reflects the aerodynamic load of generating thrust. The sequential activation protocol – baseline, electromagnetic-only, then combined electromagnetic and vibrational – enables the independent separation and quantification of each disturbance mechanism, with the resulting spectra and count-rate statistics analysed in Section 4.4.

4. Results and discussion

4.1. Energy calibration and resolution characterization

The multi-point energy calibration successfully established the operational coordinate system for the UAV spectrometer. Applying the second-order polynomial regression models (Eq. (2)) to the empirical data collected at the INPP facility yielded the precise calibration coefficients compiled in Table 3. The alignment tracking results and absolute residuals for each individual isotope calibration energy are presented in Table 4.

Table 3. Energy calibration coefficients

Parameter	Value
Zero offset, a_0 (keV)	28.465
Gain, a_1 (keV/channel)	1.342
Quadratic, a_2 (keV/channel^2)	1.553×10^{-4}
Calibration type	Manual 3-point quadratic
Calibration sources	^{241}Am, ^{137}Cs, ^{60}Co
Calibration date	5 May 2026
Maximum residual (keV)	+0.20 (at 1332.5 keV)

Table 4. Calibration reference points

Radionuclide	Channel	Reference energy (keV)	Calculated energy (keV)	Residual (keV)
^{241}Am	23.097	59.540	59.544	+0.004
^{137}Cs	448.582	661.657	661.712	+0.055
^{60}Co	881.863	1332.500	1332.699	+0.199

The maximum absolute residual of +0.20 keV observed at the highest energy boundary of 1332.5 keV yields a relative calibration error of just 0.015%. This extremely low deviation is well within the statistical limits of standard NaI(Tl) crystal performance and confirms that the electronic system linearity is highly stable and robustly mapped.

The calibration curve is shown in Figure 4, where the points indicate the reference peak centroids and the line shows the fitted quadratic function (Eq. (2)).

A representative ^{137}Cs spectrum acquired at the nominal hovering distance (200 cm), with its principal spectral features annotated, is shown in Figure 5. Critical from an operational planning perspective is the relationship between spectrum accumulation period and peak energy resolution (FWHM), presented in Table 5 and illustrated in Figure 6.

The optimal measured energy resolution of 6.19% FWHM at 661.7 keV achieved during the 300 s baseline interval strictly fulfils the internal performance requirements and surpasses the nominal manufacturer specification limit (< 7.0%).

Exploring the data in Table 5 reveals a vital engineering trade-off between flight speed and spectroscopic data quality. At a rapid sampling interval of Δt = 5 s, the counting statistics are significantly reduced, leading to increased peak uncertainty (2σ = 1.84%) and an artificial widening

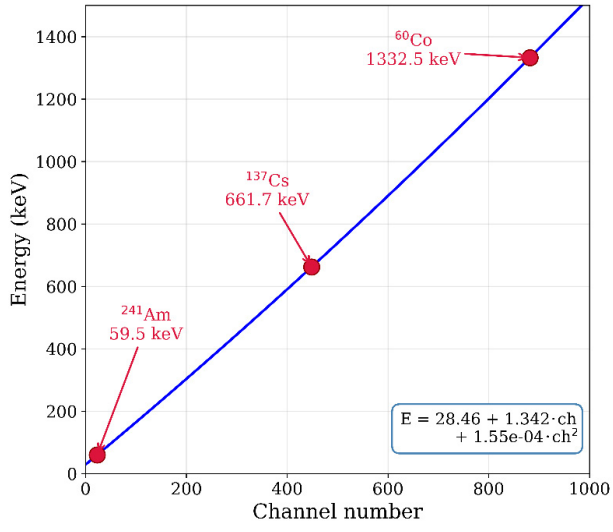


Figure 4. Energy calibration curve of the ORTEC 905-3 NaI(Tl) detector.

Table 5. Energy resolution of the ^{137}Cs peak (661.7 keV) as a function of the measurement duration (source-to-detector distance: 200 cm)

Live time (s)	Centroid (keV)	FWHM (keV)	Resolution (%)	Uncertainty 2σ (%)	Net counts
5	658.49	46.96	7.13	1.84	26,608
60	659.85	46.48	7.04	0.63	308,743
300	661.66	40.94	6.19	0.21	1,355,850

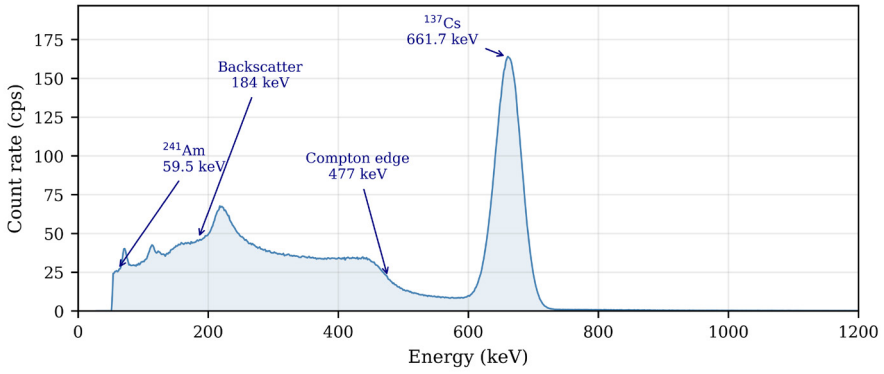


Figure 5. Gamma-ray spectrum of ^{137}Cs source (live time 300 s, source-to-detector distance 200 cm)

of the photopeak resolution to 7.13%. If a multi-rotor UAV performs a continuous strip survey at a typical ground speed of v = 4 m/s, a 5 s accumulation sequence translates to a spatial track length elongation of 20 m per spectrum.

These results clearly indicate that while a 5 s sequence is statistically sufficient for the gross detection and mapping of anomalous radiological hot-spots, high-fidelity isotopic identification and accurate background stripping operations require lower flight velocities or dedicated multi-rotor hovering states over detected points of interest to maximise counting statistics.

Note: Spectral datasets for ^{60}Co collected at extreme close contact geometry (0 cm) were excluded from the definitive FWHM calculations. True coincidence summing within close-geometry multi-cascade photon emissions introduces structural distortions to the 1173.2 keV peak profile and suppresses the 1332.5 keV net area (Gilmore & Joss, 2024). These tight-geometry profiles were therefore restricted exclusively to absolute channel centroid validation.

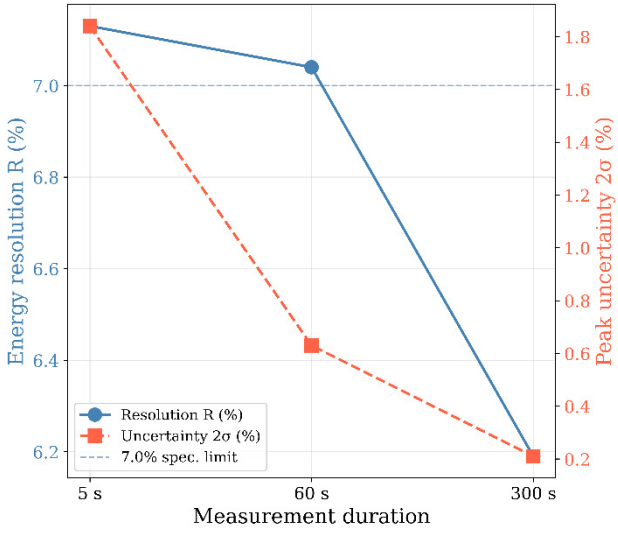


Figure 6. Effect of measurement duration on energy resolution (FWHM) and peak counting uncertainty (2σ) for the ^{137}Cs 661.7 keV peak at 200 cm source-detector distance

4.2. Absolute peak detection efficiency

The absolute full-energy peak efficiency was evaluated at the calibrated benchmark distance of 200 cm. This specific spatial geometry serves as a critical operational baseline, directly mimicking a low-altitude hovering state or a slow tactical micro-overflight of the multi-rotor UAV platform over a radiation anomaly. The primary focus was directed at ^{137}Cs (661.7 keV), which represents the primary target isotope for nuclear security screening, post-accident contamination tracking, and industrial orphan source recovery missions. The definitive empirical parameters and the resulting absolute efficiency coefficient are consolidated in Table 6.

Table 6. Absolute full-energy peak detection efficiency for ^{137}Cs (661.7 keV) at the nominal operating distance of 200 cm

Parameter	Value
Radionuclide / energy	^{137}Cs / 661.7 keV
Source activity, A (Bq)	5.034×10^{8}
Emission probability, Y_γ	0.851
Live time, t (s)	300
Source-to-detector distance (cm)	200
Net peak counts, N_net	1,355,850
Net count rate (cps)	4,520
Absolute peak efficiency, ε	1.05×10^{-5}

The calculated absolute photopeak efficiency of 1.05×10^{-5} at a 2 m distance reflects the narrow geometric solid angle subtended by the relatively compact 2'' × 2'' NaI(Tl) crystal relative to an isotropic point source. To confirm the physical validity and internal consistency of this empirical matrix, the corresponding intrinsic photopeak efficiency ε_{int} was isolated by dividing ε_{abs} by the calculated geometric fraction ($G = \Omega/4\pi$). This calculation yields an intrinsic efficiency of approximately 26%, which matches historical experimental literature profiles for identical crystal volumes exposed to 662 keV photons.

For practical flight applications, this absolute efficiency value allows the operator to determine the system's Minimum Detectable Activity (MDA). Knowing that $\varepsilon_{abs} = 1.05\times10^{-5}$, an orphan ^{137}Cs source with an activity of 1 MBq located on the ground surface will generate a net count rate of approximately 9 counts per second (cps) in the peak region when the UAV hovers directly overhead at an altitude of 2 m.

Considering standard background continuum fluctuations, this net signal guarantees a high statistical significance (>3σ) detection threshold within a brief 1–2 s integration window. However, it also highlights the system's limits: if the aircraft's flight altitude increases to 5 m or the velocity forces an off-center overflight, the sharp reduction in the solid angle will require a significantly stronger source or a slower flight speed to prevent false-negative mission profiles.

4.3. Laboratory background baseline

A long-term background characterization was executed within the INPP laboratory environment over a live acquisition period of 1802 s (30 min). This baseline measurement is highly critical to quantify the intrinsic electronic noise of the spectrometer, assess any potential localized laboratory contamination, and establish the system's ambient dead-time limit before deploying the payload onto the active multi-rotor airframe. The aggregate background continuum registered an exceptionally low dead time of just 0.07%, demonstrating that the spectroscopic module operates with superb pulse-processing efficiency and is free from initial digital saturation bottlenecks. The identified background spectral anomalies and their count rates are structured in Table 7 and Figure 7.

As shown in Table 7, the background profile is dominated by a low-energy scatter continuum with minimal counts in the high-energy regions. The natural background photopeak of ^{40}K (1460.8 keV) was not resolved within the 30-minute window due to the low-background shielding of the INPP metrology room, which suppresses external terrestrial gamma rays. Statistically extracting this weak contribution would require a significantly longer integration period. A dedicated outdoor background measurement of ≥2 hours is recommended prior to field deployment to characterize the natural gamma radiation environment relevant to UAV survey conditions. No statistically significant ^{137}Cs or ^{40}K photopeaks were observed (Figure 7).

Table 7. Background spectrum features (live time: 1802 s, dead time: 0.07%)

Energy (keV)	Count rate (cps)	Identification	Significance
59.54	8.46	^{241}Am	Ambient laboratory activity
124.09	34.17	Unidentified	Likely Pb X-ray / ^{212}Pb
661.7	< 0.20	^{137}Cs	Not statistically significant
1460.8	–	^{40}K	Below detection limit (30 min)

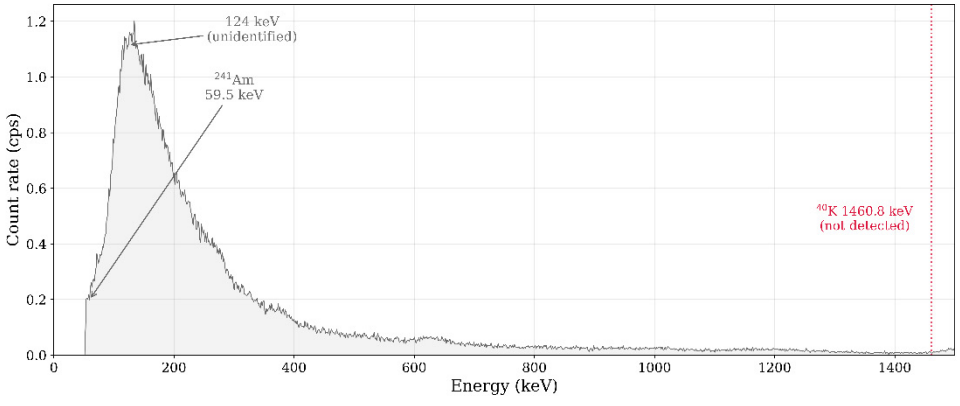


Figure 7. Laboratory background gamma-ray spectrum (live time 1802 s, dead time 0.07%)

4.4. Pre-flight validation results

The pre-flight validation assessed whether UAV motor operation perturbs the NaI(Tl) detector response under conditions representative of flight. Measurements were performed with the UAV fixed on a 2 m platform, the detector hard-mounted in its flight configuration. Three conditions were compared, each acquired in triplicate over a 600 s live time: motors off (baseline, OFF), motors running without propellers (electromagnetic interference only, EMI), and motors running with propellers fitted (combined EMI and vibration (VIB)). Throughout all measurements the detector was powered from the UAV's single battery through a regulated DC-DC converter, replicating the operational power architecture. Motors were operated at approximately 50% throttle, representative of hovering flight conditions and drawing substantial current typical of multi-rotor operation. The same energy calibration was retained for all acquisitions, and no source was present, so the comparison is based on the laboratory background spectrum.

Because the detector and propulsion system share a single power source, the measured stability represents a conservative, worst-case assessment: any conducted electrical interference propagating through the common power rail, in addition to radiated emissions from the motors, electronic speed controllers, and flight electronics, is inherently included in the test. The use of a regulated power supply further ensures that fluctuations in battery voltage during discharge do not propagate to the detector bias, eliminating supply-induced spectral drift as a confounding factor.

The total count rate remained essentially unchanged across the three conditions, as summarised in Table 8: 120.4 ± 0.7 cps (OFF), 120.2 ± 0.2 cps (EMI), and 119.9 ± 0.2 cps (VIB).

Relative to the OFF baseline, the total count rate varied by only −0.2% (EMI) and −0.4% (VIB), with all differences smaller than the inter-measurement standard deviation. The low-energy region below 200 keV – where motor-generated electromagnetic noise would be expected to manifest as a spurious count-rate increase – showed equally negligible variation (+0.1% for EMI, −0.7% for VIB). The system dead time remained below 0.01% in every condition, confirming the absence of EMI-induced detector overload or pulse pile-up.

The overlaid spectra are visually indistinguishable across the three conditions (Figure 8), and the count-rate comparison (Figure 9) confirms that all variations fall within statistical fluctuation.

These results demonstrate that, despite the shared single-battery power architecture and direct hard-mounting of the detector to the vibrating airframe, UAV motor operation induces no measurable degradation of the detector response. The absence of observable interference under these worst-case conditions provides strong evidence of system electromagnetic and mechanical robustness, indicating that neither additional electromagnetic shielding nor anti-vibration isolation is required for the present configuration.

It should be noted that energy resolution (FWHM) stability under motor operation was not quantified, as the background-only measurement provides no defined

Table 8. Detector response under pre-flight validation conditions (mean ± standard deviation, n = 3, 600 s live time each)

Condition	Total count rate (cps)	Count rate < 200 keV (cps)	Dead time (%)	Δ total vs OFF
Motors OFF (baseline)	120.4 ± 0.7	60.6 ± 0.3	< 0.01	–
Motors ON, no propellers (EMI)	120.2 ± 0.2	60.7 ± 0.0	< 0.01	−0.2%
Motors ON, propellers (EMI + vibration)	119.9 ± 0.2	60.2 ± 0.1	< 0.01	−0.4%

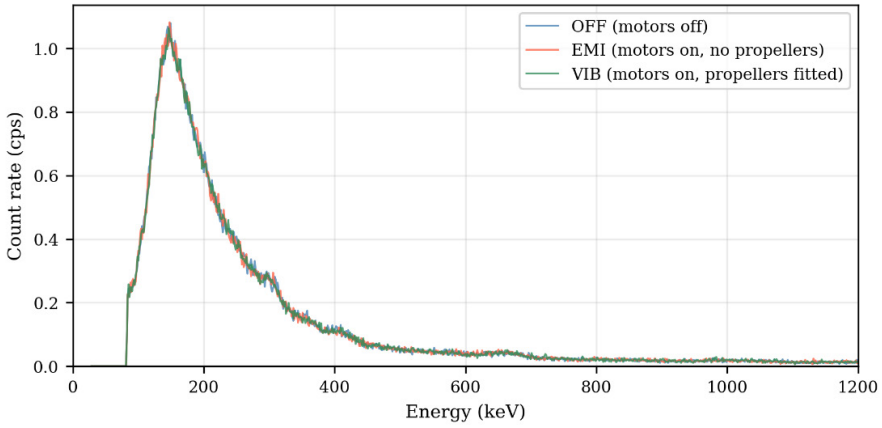


Figure 8. Overlaid background gamma-ray spectra acquired under the three pre-flight validation conditions (OFF, EMI, VIB. Mean of three 600 s acquisitions)

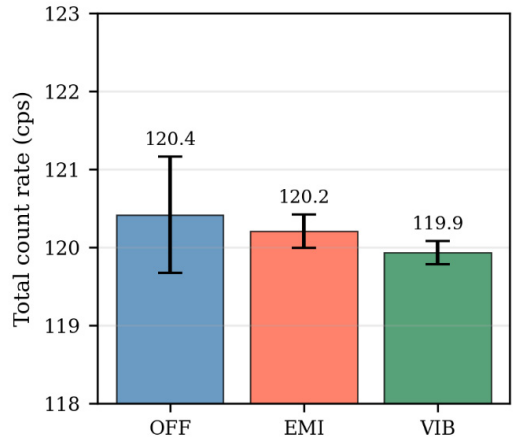


Figure 9. Total count rate under the three validation conditions (mean ± standard deviation, n = 3)

photopeak for width analysis. This assessment is identified as a priority for future work with calibrated reference sources at operational flight altitude.

4.5. Detection sensitivity and survey altitude considerations

The detection sensitivity of the system was characterised through its MDA – the lowest source activity that can be reliably distinguished from background at a stated confidence level. The MDA was evaluated for ^{137}Cs (661.7 keV), the primary target radionuclide, using the absolute detection efficiency determined in Section 4.2 and the laboratory background acquired in the operational configuration. The MDA was calculated following the Currie formulation (Currie, 1968):

$$MDA = k \cdot \sqrt{N_B} / \left(t \cdot \varepsilon \cdot Y\gamma\right), \quad (4)$$

where k = 4.65 corresponds to the 95% confidence level, N_B is the background count within the region of interest (ROI) centred on the 661.7 keV photopeak, t is the live measurement time (s), ε is the absolute full-energy peak efficiency (1.05 × 10^{-5} at 200 cm), and $Y\gamma$ = 0.851 is the gamma-ray emission probability. The ROI was defined as 661.7 keV ± one FWHM (621–703 keV), within which the measured background rate was 2.13 cps.

The MDA at the nominal operating distance of 200 cm is presented in Table 9 for several measurement durations. For a typical 300 s acquisition, the system can detect a ^{137}Cs activity of approximately 44 kBq. Extending the acquisition to 600 s lowers this to 31 kBq, reflecting the expected improvement with counting statistics.

To translate this laboratory-derived sensitivity into operational terms, the MDA was extrapolated as a function of survey altitude. Assuming point-source geometry and applying the inverse-square law to the measured 200 cm efficiency, the detection efficiency scales as (200/h)^2, where h is the source-to-detector distance in centimetres. The resulting altitude dependence (300 s acquisition) is presented in Table 10 and Figure 10, in which the dashed line marks the nominal 2 m working altitude.

The altitude dependence illustrates the fundamental trade-off in UAV-borne radiation surveying between area coverage and detection sensitivity: increasing survey altitude expands the ground footprint per pass but quadratically raises the minimum activity that can be detected. At the nominal 2 m altitude, the system detects sub-100 kBq ^{137}Cs sources within a few minutes, which is well within the activity range of typical orphan sources and localised

Table 9. Minimum detectable activity for ^{137}Cs at the nominal operating distance of 200 cm, as a function of measurement duration

Measurement time (s)	Background in ROI (counts)	MDA (kBq)
60	128	98.0
300	639	43.8
600	1277	31.0
1800	3831	17.9

Table 10. Extrapolated MDA for ^{137}Cs as a function of survey altitude (300 s acquisition, point-source geometry, inverse-square scaling)

Survey altitude (m)	Relative efficiency	MDA (kBq)	MDA (MBq)
1	4.20 × 10^{-5}	11.0	0.011
2	1.05 × 10^{-5}	43.8	0.044
3	4.67 × 10^{-6}	98.6	0.099
5	1.68 × 10^{-6}	274	0.274
10	4.20 × 10^{-7}	1096	1.10
20	1.05 × 10^{-7}	4383	4.38
30	4.67 × 10^{-8}	9861	9.86

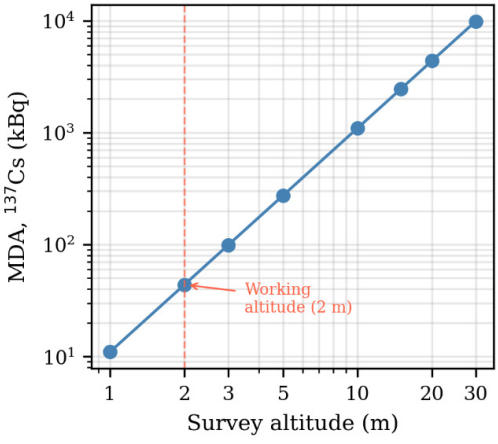


Figure 10. Extrapolated minimum detectable activity for ^{137}Cs as a function of survey altitude (300 s acquisition)

contamination. At survey altitudes of 10 m and above, only MBq-level sources remain detectable, defining the practical envelope for rapid wide-area screening versus low-altitude source confirmation.

Note: This altitude extrapolation assumes idealised point-source geometry and neglects air attenuation, which for 661.7 keV photons is small over the metre-scale distances considered ($\mu \approx 10^{-4}$ cm^{-1}) but becomes increasingly relevant at higher altitudes. Extended or shielded sources, ground scatter, and the angular response of the detector would further modify the realised sensitivity. The values therefore represent the first-order operational estimate rather than a calibrated field performance figure.

4.6. Measurement uncertainty analysis

To complement the presented results, the measurement uncertainties associated with the three metrological outputs of the calibration campaign – the energy calibration, the absolute full-energy peak efficiency, and the MDA – were evaluated following the GUM methodology, distinguishing statistical (Type A) and systematic (Type B) contributions.

For the energy calibration, the three-point quadratic model is an exact fit and therefore provides no statistical degrees of freedom. The calibration quality is instead expressed through the residuals between the reference photopeak energies and the energies reproduced by the quoted coefficients (Table 4). The maximum absolute residual is +0.20 keV at 1332.5 keV (a relative deviation of 0.015%), with a root-mean-square residual of 0.12 keV across the 59.5–1332.5 keV range. These residuals, which originate from centroid determination and coefficient rounding, are more than two orders of magnitude smaller than the detector energy resolution at 661.7 keV (FWHM = 40.9 keV) and are therefore negligible for radionuclide identification purposes.

For the absolute full-energy peak efficiency (Eq. (3)), the combined standard uncertainty was obtained by quadratic summation of the independent relative contributions listed in Table 11. The Type A contribution from counting statistics is negligible owing to the large accumulated net peak area ($N = 1.36\times10^6$ counts at 300 s). The budget is instead dominated by two Type B terms: the certified activity of the ^{137}Cs reference source and the source–detector positioning tolerance, bounded by the ±2.5% inverse-square-law deviation of the calibration rig. The combined standard uncertainty of the efficiency is 3.9%, corresponding to an expanded uncertainty of 7.8% at the approximately 95% confidence level (k = 2). The efficiency is accordingly reported as $\varepsilon = (1.05 \pm 0.04) \times 10^{-5}$.

For the minimum detectable activity, two distinct sources of uncertainty must be separated. First, the Currie formulation itself (Eq. (4)) employs the coverage factor k = 4.65, so the reported MDA values are by construction 95% confidence thresholds ($\alpha = \beta = 0.05$) rather than point estimates. Second, because the MDA is inversely proportional to the detection efficiency, the 3.9% efficiency uncertainty propagates linearly into the derived activity values. For the reference condition (300 s, 200 cm) this corresponds to MDA = 43.8 ± 1.7 kBq. The altitude-extrapolated values (Table 10) additionally carry a model uncertainty associated with the idealised point-source, attenuation-free, and scatter-free assumptions of the inverse-square scaling. This contribution is not quantified here and is addressed qualitatively in the Discussion.

5. Discussion

The results confirm that the developed UAV-borne NaI(Tl) system meets the metrological requirements for environmental gamma surveying and, critically, that this performance is preserved once the detector is integrated into the UAV platform. The energy calibration, resolution, and photopeak efficiency obtained in the integrated configuration are consistent with values expected for a 2″ × 2″ NaI(Tl) detector, satisfying the central objective of the methodological framework.

A pertinent question is how closely the bench-test conditions approximate genuine flight. With respect to electromagnetic interference, the bench configuration is expected to be fully representative: in flight the detector operates with the same power architecture, the same motor controllers, and comparable phase currents to the hovering throttle (~50%) reproduced in the test, so the in-flight electrical environment differs little from the one validated. The eighteen-fold increase in current draw between the EMI and VIB conditions (1.87 A to 34.4 A mean) produced no measurable spectral effect, indicating a substantial interference margin. The vibration environment is reproduced more approximately. In the bench test the thrust-loaded airframe was rigidly restrained, so structural vibration was transmitted to the detector mount

Table 11. Uncertainty budget of the absolute full-energy peak efficiency for the ^{137}Cs photopeak (661.7 keV) at 200 cm

Uncertainty component	Type	Relative standard uncertainty (%)
Counting statistics of the net peak area ($N = 1.36\times10^6$)	A	0.09
Certified activity of the reference source	B	3.0
Gamma-ray emission probability ($Y_\gamma = 0.851$)	B	0.2
Source–detector positioning (inverse-square deviation)	B	2.5
Combined standard uncertainty, $u_c(\varepsilon)/\varepsilon$	–	3.9
Expanded uncertainty, U (k = 2, ≈95% confidence)	–	7.8

essentially undamped, whereas a free-flying airframe dissipates part of this energy as rigid-body motion. In this respect the bench condition is plausibly conservative for high-frequency motor-induced excitation, while low-frequency manoeuvre loads, gust response, and landing shocks remain outside the tested envelope. Two further factors are unique to flight: convective cooling and ambient temperature variation, to which the NaI(Tl) light yield is sensitive at approximately − 0.2 – 0.3% per °C (Knoll, 2010), and the continuously varying source–detector geometry. The former motivates continuous monitoring of the photopeak position during the planned flight trials. The latter is a survey-methodology issue rather than a detector-stability one and is handled at the data-processing level through altitude correction (Eq. (1)).

The most significant operational finding is the absence of measurable degradation of the detector response under motor operation. Whereas electromagnetic interference from motors and electronic speed controllers, and vibration transmitted through the airframe, have been identified as potential sources of spectral degradation in UAV-mounted detectors the present system showed no such effect. Because the detector and propulsion system share a single power source through a regulated converter, the test inherently captured both radiated and conducted interference, making the observed stability a conservative result. The practical implication is that neither supplementary electromagnetic shielding nor active anti-vibration isolation is required for this configuration – simplifying system design and reducing payload mass, both advantageous for endurance-limited multi-rotor platforms.

The detection-sensitivity analysis frames the system's capability in operational terms. At the nominal 2 m operating altitude, the system detects ^{137}Cs activities on the order of tens of kilobecquerels within a few minutes, well matched to the detection of orphan sources and localised contamination. The strong inverse-square dependence of sensitivity on altitude quantifies the fundamental trade-off in airborne surveying – greater altitude increases the ground area covered per pass but raises the minimum detectable activity quadratically – providing a direct basis for mission planning, consistent with the altitude dependence reported for other UAV gamma-survey systems (Bunn et al., 2022).

The altitude extrapolation of the MDA warrants quantitative qualification, as it rests on three idealisations. First, atmospheric attenuation was neglected: applying the attenuation term of Eq. (1) with $\mu \approx 9.3 \times 10^{-3}$ m^{-1} for air at 662 keV, the omission is negligible at the 2 m reference distance (<2%) but reaches approximately 10% at 10 m and 30% at 30 m, so the tabulated values progressively understate the true MDA at survey altitudes. Second, the point-source assumption defines the applicability domain: for spatially distributed contamination the photon fluence decreases with altitude far more slowly than the inverse square – in the limiting case of an extended planar source the geometric term becomes nearly altitude-independent – so the extrapolation is strictly applicable to compact (orphan-source) geometries and conservative for distributed sources. Third, the laboratory background underlying the Currie term differs from the open-field radiation environment, where terrestrial radionuclides and ground-scattered photons elevate the continuum beneath the 662 keV window and would raise the operational MDA accordingly. The extrapolated values should therefore be read as the first-order mission-planning estimates, with empirical confirmation at altitude, using calibrated reference sources, assigned to the planned flight campaign.

Several limitations define the scope of this validation and the direction of future work. Energy-resolution stability under motor operation was not quantified, as the background-only measurement provides no defined photopeak for width analysis. The detection efficiency was determined only for ^{137}Cs at 662 keV rather than across a full energy-dependent curve the quantitative implications of the assumptions underlying the altitude extrapolation of the MDA were examined above. Finally, all measurements were performed under controlled static conditions, so the influence of flight dynamics was outside the present scope. These limitations motivate a future flight campaign with calibrated reference sources at operational altitudes, enabling direct measurement of resolution stability under genuine flight vibration, a full efficiency calibration, and empirical validation of the extrapolated MDA – advancing the system from a metrologically validated platform towards a fully operational surveying tool.

6. Conclusions

This study developed and methodologically validated a UAV-borne NaI(Tl) gamma-ray spectrometry system for environmental radiation surveying. The main contribution is a replicable end-to-end framework that documents the complete development pipeline – from traceable characterisation at an accredited calibration laboratory, through integration into a custom multi-rotor platform, to structured pre-flight verification under simulated operational conditions – a pipeline that is rarely reported in full in the published literature, where systems are typically presented only in their final flight-qualified state.

The novelty of the work lies in the proposed pre-flight validation protocol. Three sequential operating conditions – motors off, motors energised without propellers, and motors under aerodynamic load with propellers fitted – allow the electromagnetic and vibrational disturbance mechanisms to be isolated and quantified independently, while the deliberate single-battery architecture, in which the detector and the propulsion system share one power source through a regulated converter, captures both radiated and conducted interference in a worst-case configuration. This conservative, mechanism-resolving protocol distinguishes the present validation from existing studies, which generally assess integrated detector performance only in flight, where the individual contributions of EMI and vibration cannot be separated.

The key quantitative findings are as follows. The three-point quadratic energy calibration reproduced all reference energies within +0.20 keV (0.015%). The energy resolution of 6.19% FWHM at 661.7 keV satisfies the <7% specification and the absolute photopeak efficiency at the nominal 2 m operating distance was determined as $(1.05 \pm 0.04) \times 10^{-5}$. Under motor operation, the total count rate changed by less than 0.4% and the dead time remained below 0.01%, demonstrating that the detector requires neither supplementary electromagnetic shielding nor anti-vibration isolation. From an aviation-integration perspective this is the central practical outcome: avoided shielding mass and mechanical complexity translate directly into extended flight endurance – the binding constraint of multi-rotor survey operations. The minimum detectable activity of 43.8 ± 1.7 kBq for ^{137}Cs (300 s, 2 m), scaling quadratically with altitude, quantifies the coverage–sensitivity trade-off that governs survey mission planning.

In practical terms, the validated system is suited to orphan-source recovery, post-accident contamination mapping, and routine environmental surveillance, with the reported sensitivity–altitude relationship providing a direct quantitative input for flight-mission design. Future work will extend the validation to flight campaigns with calibrated reference sources at operational altitudes, enabling direct measurement of energy-resolution stability under genuine flight vibration, a full energy-dependent efficiency calibration, and empirical confirmation of the extrapolated detection limits – advancing the system from a metrologically validated payload towards routine operational deployment.

Acknowledgements

The authors gratefully acknowledge the accredited Verification and Calibration Laboratory of the Ignalina Nuclear Power Plant (INPP) for providing access to the UPGD-2M-D gamma calibration facility and for technical support during detector characterisation.

Author contributions

Conceptualization, J. M.; methodology, J. M., L. A. and D. P.; investigation, J. M., A. P., L. A. and D. P.; formal analysis, J. M.; writing – original draft preparation, J. M.; writing–review and editing, D. J.; supervision, J. M. All authors have read and agreed to the published version of the manuscript.

Disclosure statement

No potential conflict of interest was reported by the authors.

References

Ardiny, H., Beigzadeh, A., & Mahani, H. (2024). Applications of unmanned aerial vehicles in radiological monitoring: A review. *Nuclear Engineering and Design*, *422*, Article 113110. https://doi.org/10.1016/j.nucengdes.2024.113110

Bunn, A., Wagner, K., Fagan, D., Gadey, H., Ikenberry, T., Markham, K., & Obiri, M. (2022). *Drones for decommissioning proof-of-concept*. Pacific Northwest National Laboratory. https://doi.org/10.2172/1923755

Connor, D. T., Wood, K., Martin, P. G., Goren, S., Megson-Smith, D., Verbelen, Y., Chyzhevskyi, I., Kirieiev, S., Smith, N. T., Richardson, T., & Scott, T. B. (2020). Radiological mapping of post-disaster nuclear environments using fixed-wing unmanned aerial systems: A study from Chornobyl. *Frontiers in Robotics and AI*, *6*. https://doi.org/10.3389/frobt.2019.00149

Corbacho, J. A., Baeza, J. A., & Caballero, J. M. (2024). Use of a drone-based gamma-ray spectrometry system to assess point or extended radioactive sources. *Radioprotection*, *59*(2), 80–87. https://doi.org/10.1051/radiopro/2023039

Currie, L. A. (1968). Limits for qualitative detection and quantitative determination. Application to radiochemistry. *Analytical Chemistry*, *40*(3), 586–593. https://doi.org/10.1021/ac60259a007

Geelen, S., Camps, J., Olyslaegers, G., Ilegems, G., & Schroeyers, W. (2022). Radiological surveillance using a fixed-wing UAV platform. *Remote Sensing*, *14*(16), Article 3908. https://doi.org/10.3390/rs14163908

Gilmore, G. R., & Joss, D. (2024). *Practical Gamma-ray Spectrometry*. Wiley. https://doi.org/10.1002/9781394286577

Gong, P., Tang, X.-B., Huang, X., Wang, P., Wen, L.-S., Zhu, X.-X., & Zhou, C. (2019). Locating lost radioactive sources using a UAV radiation monitoring system. *Applied Radiation and Isotopes*, *150*, 1–13. https://doi.org/10.1016/j.apradiso.2019.04.037

International Atomic Energy Agency. (2022). *Technical output from the technical meeting use of uncrewed aeriel systems (UAS) for radiation detection and surveillance*. https://inis.iaea.org/records/xpyjv-zkb05

International Atomic Energy Agency. (2026). *IAEA Incident and Trafficking Database (ITDB) Factsheet*. https://www.iaea.org/sites/default/files/25/03/itdb-factsheet.pdf

Jiang, J., Shimazoe, K., Nakamura, Y., Takahashi, H., Shikaze, Y., Nishizawa, Y., Yoshida, M., Sanada, Y., Torii, T., Yoshino, M., Ito, S., Endo, T., Tsutsumi, K., Kato, S., Sato, H., Usuki, Y., Kurosawa, S., Kamada, K., & Yoshikawa, A. (2016). A prototype of aerial radiation monitoring system using an unmanned helicopter mounting a GAGG scintillator Compton camera. *Journal of Nuclear Science and Technology*, *53*(7), 1067–1075. https://doi.org/10.1080/00223131.2015.1089796

Knoll, G. F. (2010). *Radiation detection and measurement*. Wiley.

Kunze, C., Preugschat, B., Arndt, R., Kandzia, F., Wiens, B., & Altfelder, S. (2022). Development of a UAV-based gamma spectrometry system for natural radionuclides and field tests at Central Asian Uranium Legacy Sites. *Remote Sensing*, *14*(9), Article 2147. https://doi.org/10.3390/rs14092147

MacFarlane, J. W., Payton, O. D., Keatley, A. C., Scott, G. P. T., Pullin, H., Crane, R. A., Smilion, M., Popescu, I., Curlea, V., & Scott, T. B. (2014). Lightweight aerial vehicles for monitoring, assessment and mapping of radiation anomalies. *Journal of Environmental Radioactivity*, *136*, 127–130. https://doi.org/10.1016/j.jenvrad.2014.05.008

Martin, P. G., Connor, D. T., Estrada, N., El-turke, A., Megson-Smith, D., Jones, C. P., Kreamer, D. K., & Scott, T. B. (2020). Radiological identification of near-surface mineralogical deposits using low-altitude unmanned aerial vehicle. *Remote Sensing*, *12*(21), Article 3562. https://doi.org/10.3390/rs12213562

Martin, P. G., Kwong, S., Smith, N. T., Yamashiki, Y., Payton, O. D., Russell-Pavier, F. S., Fardoulis, J. S., Richards, D. A., & Scott, T. B. (2016). 3D unmanned aerial vehicle radiation mapping for assessing contaminant distribution and mobility. *International Journal of Applied Earth Observation and Geoinformation*, *52*, 12–19. https://doi.org/10.1016/j.jag.2016.05.007

Sanada, Y., Orita, T., & Torii, T. (2016). Temporal variation of dose rate distribution around the Fukushima Daiichi nuclear power station using unmanned helicopter. *Applied Radiation and Isotopes*, *118*, 308–316. https://doi.org/10.1016/j.apradiso.2016.09.008

Sanada, Y., & Torii, T. (2015). Aerial radiation monitoring around the Fukushima Dai-ichi nuclear power plant using an unmanned helicopter. *Journal of Environmental Radioactivity*, *139*, 294–299. https://doi.org/10.1016/j.jenvrad.2014.06.027

Schraml, S., Hubner, M., Taupe, P., Hofstätter, M., Amon, P., & Rothbacher, D. (2022). Real-time gamma radioactive source localization by data fusion of 3D-LiDAR terrain scan and radiation data from semi-autonomous UAV flights. *Sensors*, *22*(23), Article 9198. https://doi.org/10.3390/s22239198

Towler, J., Krawiec, B., & Kochersberger, K. (2012). Radiation mapping in post-disaster environments using an autonomous helicopter. *Remote Sensing*, *4*(7), 1995–2015. https://doi.org/10.3390/rs4071995

Vetter, K., Barnowksi, R., Haefner, A., Joshi, T. H. Y., Pavlovsky, R., & Quiter, B. J. (2018). Gamma-Ray imaging for nuclear security and safety: Towards 3-D gamma-ray vision. In *Nuclear Instruments and Methods in Physics Research*, *Section A*: *Accelerators*, *Spectrometers*, *Detectors and Associated Equipment* (Vol. 878, pp. 159–168). Elsevier B.V. https://doi.org/10.1016/j.nima.2017.08.040